Build Simul
https://doi.org/10.1007/s12273-018-0461-9

Computational modeling of natural ventilation in low-rise non-rectangular floor-plan buildings

Juan M. Gimenez[1,2] (✉), Facundo Bre[1,3], Norberto M. Nigro[1,2], Victor Fachinotti[1,2]

1. Centro de Investigación de Métodos Computacionales (CIMEC), UNL, CONICET, Predio "Dr. Alberto Cassano", Colectora Ruta Nacional 168 s/n, 3000, Santa Fe, Argentina

2. Facultad de Ingeniería y Ciencias Hídricas - Universidad Nacional del Litoral, Ciudad Universitaria, Paraje "El Pozo", Santa Fe, Argentina

3. Facultad Regional Concepción del Uruguay (FRCU), Universidad Tecnológica Nacional (UTN), 3260, Concepción del Uruguay, Argentina

Abstract

Natural ventilation (NV) is a relevant passive strategy for the design of buildings in seek of energy savings and the improvement of the indoor air quality and the thermal comfort. The main aim of this work is to present a comprehensive NV modeling study of a non-rectangular floor-plan dwelling. Given the arbitrary shape of the building, recourse is made to computational fluid dynamics (CFD) to determine the surface-averaged pressure coefficients ($\overline{C_p}$). The CFD model was calibrated to match experimental data from an extensive wind tunnel database for low-rise buildings. Then, $\overline{C_p}$ computation via CFD is used to feed the building performance simulation software EnergyPlus, in replacement of the built-in Swami and Chandra parametric model that is only valid for estimating $\overline{C_p}$ in rectangular floor-plan buildings. This computational tool is used to investigate the effect of NV on the thermal performance and the airflow rate in a social housing located in the Argentine Littoral region. Simulation results of the considered building show that NV enables to reduce even more than 65% of the cooling degree-hours. Furthermore, regarding to the $\overline{C_p}$ source (either CFD or Swami and Chandra's), it is also found that this data has a considerable effect on the airflow rates, but a little effect on the thermal performance.

Keywords

natural ventilation,
airflow network model,
pressure coefficient,
computational fluid dynamics,
building performance simulation,
EnergyPlus

Article History

Received: 12 March 2018
Revised: 2 July 2018
Accepted: 4 July 2018

1 Introduction

According to the fifth assessment report of the Intergovernmental Panel on Climate Change (2014), the temperature will be 2 to 4.5 °C higher by 2100 (referred to 2014) in Southeastern South America (SESA). Filippín et al. (2017), after a retrospective analysis of the energy consumption of single-family dwellings in the central region of Argentina, estimated that the energy demands by 2039 will decrease in winter periods and will increase in summer periods.

The natural ventilation (NV) showed to be a powerful passive strategy to save energy and improve thermal comfort throughout the world (Oropeza-Perez and Østergaard 2014; Sorgato et al. 2016; Chen et al. 2017). Specific to SESA, Invidiata and Ghisi (2016) recommended the use of NV in future home designs to reduce the effects of global warming. At Buenos Aires city (in central Argentina), a significant potential of 4514 NV hours was observed by Chen et al. (2017). So, NV is expected to greatly contribute to alleviate the current Argentine electrical energy crisis (Sarinelli and Clucellas 2015) and future challenges due to climate change. Beyond the relevant reduction of energy consumption, NV also improves quality of life. The acceptable thermal comfort range for naturally ventilated buildings is larger than for buildings with standard mechanical HVAC systems (de Dear and Brager 2002). Also, the medical condition known as the sick building syndrome in people working or living in air-conditioned buildings was reported to be more prevalent than in those living or working in naturally ventilated buildings (Seppänen and Fisk 2002).

In building design, in order to take into account the effect of NV on occupant comfort, it is necessary to quantify the naturally driven ventilation rates. This task requires a

E-mail: jgimenez@cimec.unl.edu.ar

deep knowledge and an accurate prediction of coupled airflow and heat transfer. The main tool to this end is computational simulation. Computational fluid dynamics (CFD) is the preferred tool when spatially detailed information is required; it has been used to simulate NV under a variety of conditions, including wind- and/or buoyancy-driven flows (Zhai 2014). However, in the context of building performance simulation (BPS), where an annual simulation of the entire building is required, CFD simulation is unaffordable due to the computational time. To quickly predict airflows throughout an entire building, several reduced-order airflow models have been developed. A comprehensive literature review was given by Zhai et al. (2015), who concluded that analytical models are only applicable to specific geometries and driving forces (i.e., single zone with one or multiple openings), while the numerical solution of a nonlinear equation system is required for more complex scenarios (like multizone airflows). Among the available options for multizone airflows, Zhai et al. (2015) recommended the use of the airflow network models (AFN).

A crucial information for AFN in BPS is the wind-induced pressure distribution on the building surfaces, which is generally characterized by the wind pressure coefficient (C_p). Being associated with air change rate, this is a relevant parameter in energy consumption, thermal comfort, and air quality of buildings. It is defined as the dimensionless ratio between the dynamic pressure measured at a point of the building façade, i.e. the difference between the static pressure p at the point and a static reference pressure p_∞ at freestream (i.e., far away from any disturbance), and the dynamic pressure of the air flow (wind) in the freestream; mathematically,

$$C_p = \frac{p - p_\infty}{\frac{1}{2}\rho U_H^2} \quad (1)$$

where ρ is the air density and U_H is the freestream wind speed, which is often taken at the building height H in the upstream undisturbed flow. The dynamic pressure (and hence C_p) depends on several parameters like building geometry, façade detailing and position, urban surroundings and wind speed and direction. Given the complexity of C_p spatial variation, BPS and AFN incorporate it in a simplified way, usually through the surface-averaged value ($\overline{C_p}$) (Cóstola et al. 2009).

In order to determine $\overline{C_p}$, most BPS-AFN programs make use of secondary data sources like databases (Orme and Leksmono 2002; ASHRAE 2009) and analytical models calibrated with experimental measurements (Swami and Chandra 1988; Muehleisen and Patrizi 2013; Grosso 1992). Particularly, the BPS software EnergyPlus (from now on referred as E+) (Crawley et al. 2001) uses by default the analytical model proposed by Swami and Chandra (1988). The main drawback of secondary data sources is that their limitation to rectangular floor-plan buildings. Because of this, several authors limited the reach of their works and conclusions (Breesch and Janssens 2010; Ramponi et al. 2014; Rackes et al. 2016; Bre and Fachinotti 2017). Recently, Bre et al. (2018) proposed a methodology based on artificial neural networks to predict $\overline{C_p}$ data for low-rise buildings with different kinds of roofs, which was shown to be more accurate than the popular analytical models. However, its extension is not envisaged to completely arbitrary shapes.

So, until now, when the building has an arbitrary topology, a primary data source has to be used to obtain C_p values. A first option is to perform a wind-tunnel measurement. However, this alternative is rarely employed during the design of a specific building because of its high cost and the involved know-how. The second option consists of using CFD to predict the external flow, which has been recognized as a reliable tool for C_p computation (Cóstola et al. 2009; Montazeri and Blocken 2013; Ntinas et al. 2018; Yi and Feng, 2013). However, up to the authors' knowledge, neither the use of CFD to compute $\overline{C_p}$ nor the use of the such-computed $\overline{C_p}$ to feed BPS-AFN simulations has a precedent in literature.

Therefore, in the search for evaluating NV in non-rectangular floor-plan low-rise buildings, a comprehensive CFD-BPS pipeline is proposed as the aim of this work.

According to Hong et al. (2018), one of the current ten challenges is the use of BPS to support government decision making on building efficiency research, technology development and assessment. In this context, and to measure the NV potential of the Argentine Littoral region, a social dwelling located in Paraná city is chosen as the case study. Social houses are not expected to be artificially air conditioned. Then, BPS must include NV and its effect on the occupant comfort. So, the coupled thermal-airflow model for BPS is presented, introducing the requirement of $\overline{C_p}$ data (Section 2).

Because of the non-standard shape of the building analyzed, CFD simulations are used to determinate $\overline{C_p}$ (Section 3). The best suited CFD model is determined through comparison to the experimental wind tunnel database for low-rise buildings from the Tokyo Polytechnic University (TPU) (Quan et al. 2007). The choice of the turbulence model conducting to a best match of the experimental results is deeply discussed, with the target of being useful as reference for future works in the area.

Once obtained the $\overline{C_p}$ data, coupled thermal-airflow simulations are performed for the case study using the E+ software along with its AFN module (Section 4). The impact of using NV in this particular building in terms of predicted airflows and thermal comfort is analyzed and discussed, highlighting the differences between predictions obtained using CFD-computed $\overline{C_p}$ and analytical $\overline{C_p}$ calibrated for simpler building shapes.

Finally, the relevant conclusions and future works are pointed out (Section 5).

2 Natural ventilation modeling

In order to simulate the evolution of the thermal behavior along a year, the building energy simulation program E+ employs a coupled thermal-airflow approach, where the heat balance is coupled with the airflow balance following an iterative process.

Assuming that the indoor temperature T is well mixed and in absence of air conditioning systems, the thermal energy balance in a thermal zone is given by

$$\rho c_p V \frac{dT}{dt} = E_{conv} + E_{int} + E_{vent} \tag{2}$$

where ρ is the air density, c_p is the specific heat capacity, V is the volume of the zone; the left hand side defines the energy stored in the thermal zone, which is equal to the sum of three terms: the convective heat transfer from the surfaces (E_{conv}), the convective internal loads (E_{int}) and the heat transfer due to outside air infiltrations mainly by NV (E_{vent}), respectively. E+ uses by default a third order finite difference approximation of the temporal derivative in Eq. (2), but alternatively an analytic exponential-like solution can be invoked.

In this work, NV is accounted for using a multizone airflow network model, where the building is considered to be a group of well-mixed zones (or nodes), connected by flow paths (Walton 1989). External nodes are also included to characterize the outdoor conditions on each façade of the building. This model is available in E+ through the module Airflow Network (AFN) (Gu 2007).

At the zone or node i, which has N airflow paths, the NV-induced heat transfer is

$$E_{vent} = \rho c_p \sum_{j=1}^{N} Q_{ij}(T_i - T_{out}) \tag{3}$$

where T_i is the temperature of node i, and T_{out} is the outdoor temperature, and Q_{ij} is the volumetric flow rate from node i to node j, which is calculated as

$$Q_{ij} = C_d W_{eff} \int_{z_0}^{z_r} v(z) dz \tag{4}$$

where z_0 denotes the height of the bottom of the opening, z_r that of the top of the opening, C_d is the discharge coefficient, W_{eff} is the effective opening width (accounting for the opening factor), and $v(z)$ is the air velocity at the level z, given by

$$v(z) = \sqrt{\frac{2\Delta P_{ij}(z)}{\rho}} \tag{5}$$

being ΔP_{ij} the total pressure difference across the opening between nodes i and j.

At its turn, ΔP_{ij} is defined by the Bernoulli equation as

$$\Delta P_{ij} = P_i - P_j + P_S + P_W \tag{6}$$

where P_i and P_j are the total pressures at nodes i and j (to be determined); P_S is the pressure difference due to density and height, given by

$$P_S = \rho g(z_i - z_j) \tag{7}$$

where g is the gravity acceleration, z_i and z_j are the elevations of nodes i and j, respectively; and P_W is the pressure induced by wind on the building envelope openings, given by

$$P_W = \frac{1}{2} C_p \rho U^2 \tag{8}$$

where U is the wind speed at a reference height and C_p is the pressure coefficient which depends on the location on the building surface and the wind direction.

Reliable wind pressure coefficients are key input parameters for air infiltration and ventilation studies. Usually, building energy simulation and stand-alone airflow network programs provide and/or use simplified C_p data. An important simplification, to be adopted in this work, consists of using surface-averaged C_p, say $\overline{C_p}$, instead of local C_p with a high resolution in space. Cóstola et al. (2010) considered $\overline{C_p}$ a reliable estimator of $\overline{C_p}$ although it could introduce a high uncertainty in airflow rate calculation.

By default, E+ computes $\overline{C_p}$ using the analytical expression proposed by Swami and Chandra (1988), from now on referred to as the S&C formula, which was calibrated on the base of experimental measurements for rectangular floor-plan buildings. For buildings with more complex shapes, S&C results are generally poor. For such buildings, C_p can be obtained from wind tunnel experiments. However, this option is rarely employed during the design of a specific building due to its high cost and the high level of know-how involved. As an affordable alternative, several works propose CFD for C_p computing (Cóstola et al. 2009;

Montazeri and Blocken 2013), approach that is followed in this work. To obtain reliable data with CFD also requires a high level of know-how about the simulation settings, and data pre- and post-processing. The next section is devoted to detail the current CFD methodology for $\overline{C_p}$ computation.

3 Computing surface-averaged C_p using CFD

The turbulence modeling is crucial for the accurate prediction of C_p using CFD. It is well known that the Large Eddy Simulation (LES) model leads to better accuracy than the Reynolds-averaged Navier–Stokes (RANS) one (Murakami 1998). However, the computational time required by LES is one or two orders of magnitude larger than that of RANS, that is, weeks for LES versus days or hours for RANS in problems on typical buildings. This makes LES usually unaffordable for non-academic purposes like engineering consulting or building design.

So, RANS is the chosen turbulence model in this work. The most popular RANS model, that is the standard k-ϵ, is not suitable for the accurate prediction of the flow behavior around bodies with sharp edges like most of the buildings (Murakami et al. 1990; Montazeri and Blocken 2013). This is mainly because the standard k-ϵ overestimates the production of turbulent kinematic energy k around the frontal corner of the roof. Some authors proposed modified k-ϵ models to fix it. Kato and Launder (1993) proposed a revised k-ϵ model, the KL model, to eliminate the excessive production of k around a stagnation point. Tsuchiya et al. (1997) presented the MMK model which was born as an improvement of the k-ϵ model for flow and pressure fields around a bluff body. Both models improve the C_p prediction on the roof and on the wind impinging side, but are not good to predict pressures in wind wake zones.

Montazeri and Blocken (2013) presented a validation and a sensitivity analysis of CFD simulation of wind-induced pressure coefficients on buildings with and without balconies. They found that RANS models, in spite of their limitations, were suitable to predict the wind-induced mean pressures at windward building façades, but larger deviations were obtained for wind pressures on the leeward façade, especially for oblique wind. Recently, Tominaga et al. (2015) made a study of the airflow around isolated gable-roof buildings with different roof pitches comparing wind tunnel experiments and CFD simulations. There, employing various k-ϵ models and the k-ω shear stress transport (SST) turbulence model, they found that the deviation between the velocity and turbulent energy results of the simulation and the measured results was 30% for the worst case, that in the lower wind speed region behind the building. Regarding pressure coefficients, they also observed the overestimation of the turbulent kinetic energy around the corner of the roof and its incidence on C_p prediction. However, they tested neither the ad-hoc turbulence models developed to mitigate that effect nor the variation of the results depending on the wind incidence angle. On the other hand, Ntinas et al. (2018) evaluated k-ϵ family turbulence models for simulating external airflow around various building roofs with tunnel experiments. They found a reasonable mean agreement concerning the velocity and the turbulence kinetic energy but high prediction error on buildings' roofs. In general, in none of these previous works, it was possible to predict the pressure distribution with an acceptable accuracy for all building surfaces (or at least all the sides), which is the most important requirement for the purpose of the current work, since the airflow through a building depends on the indoor–outdoor pressure differences.

So, uncertainty still remains in the literature concerning the appropriate RANS turbulence model to accurately predict $\overline{C_p}$ values for generally isolated low-rise buildings. In order to determine a methodology for the prediction of $\overline{C_p}$ in buildings using CFD, in this work a comprehensive and systematic computation of $\overline{C_p}$ on each building surface using various 3D RANS models is presented. A wide number of CFD results is obtained and then compared to the experimental database from the Wind Engineering Information Center of the Tokyo Polytechnic University (TPU) (Quan et al. 2007) in order to determine which RANS models are the best suited for several wind incidence angles and type of roofs (flat, gable and hip-roofed).

The so-selected RANS turbulence model is part of a complete CFD methodology, to be described later in this section, which allows computing accurate $\overline{C_p}$ results for all surfaces of low-rise buildings with two main purposes: i) to employ these data in BPS analysis of the case study target of this work, and ii) as a long-term objective, to generate $\overline{C_p}$ databases for complex building shapes like L-shape, U-shape, etc.

This section defines the methodology proposed to evaluate the accuracy of $\overline{C_p}$ prediction in low-rise buildings using CFD. Subsection 3.1 describes the experimental database that served to validate the numerical results, together with the chosen study cases. Subsection 3.2 details the CFD modeling, including the mathematical formulation of the fluid dynamics problem and the selected numerical tool, the turbulence models chosen, a detailed information about the computational domain and its discretization, the boundary conditions and solver settings used. Finally, Subsection 3.3 reports and discusses the results of CFD simulations concluding in the selection of the most accurate turbulence model for this kind of problems.

3.1 Description of wind tunnel experiments

The database selected to compare the CFD simulations is, from now on, referred to as the TPU database. For the wind tunnel measurements, they used a 0.1 m cubic building model for the case of an isolated low-rise building setting a length scale of 1/100. A potential law profile adjusts the wind field used in experiments with a mean wind velocity profile exponent of 0.20 and a gradient height of 450 m, while the turbulence density at a height of 10 cm was 0.25. The test wind velocity at this height was 7.4 m/s, corresponding to 22.4 m/s at a height of 10 m in full scale. During the experiments, three types of models were tested: flat-, gable-, and hip-roofed. Also, several height/breadth (H/B) and depth/breadth (D/B) ratios and pitches for sloped roofs were analyzed. Figure 1 presents the building models and the nomenclature for sizes, angles, and surface numbering.

The TPU database includes thousands of contours of statistical values of local wind pressure coefficients, hundreds of graphs of statistical values of area-averaged wind pressure coefficients on the roof and wall surfaces, and time-series data of point wind pressure coefficients for almost one thousand test cases. The $\overline{C_p}$ data on the building surfaces (walls and roofs) are presented as plots of mean-surface pressure according to the wind attack angle from 0° to 90° in 15° increments.

According to the targets of this work, six building configurations from the TPU database were selected to be compared with CFD simulations. Only the extreme depth-to-breadth and height-to-breadth ratios (D/B = 3:2 and H/B =1:4, respectively) are selected, avoiding the standard cases already dealt with in previous works (Wright and Easom 2003; Cóstola et al. 2009) (as an example, the MMK turbulence model was explicitly developed for solving flat roof with 1:1 ratios). The three roof types, that is flat, gable-roofed and hip, are tested, considering the gable and the hip roof angle β = 45°. Also, two wind incidence angles are selected (θ = 0° and θ = 45°), giving raise to a total of 6 cases to compare experimental and numerical data.

3.2 CFD modeling

Mathematical model formulation. The flow in the atmospheric boundary layer (ABL) environments can be considered as an incompressible homogeneous viscous flow with constant density ρ and kinematic viscosity ν. Governing equations are the RANS equations which are obtained considering that any quantity, for instance the velocity $\mathbf{u}$, is decomposed into its time-averaged and fluctuating parts, i.e. $\mathbf{u} = \overline{\mathbf{u}} + \mathbf{u}'$. This decomposition is used in the standard Navier–Stokes equations and, after a time averaging, it leads to the equation system given by

$$\nabla \cdot \overline{\mathbf{u}} = 0 \tag{9}$$

$$\frac{\partial \overline{\mathbf{u}}}{\partial t} + \left(\overline{\mathbf{u}} \cdot \nabla \overline{\mathbf{u}}\right) = -\frac{1}{\rho}\nabla \overline{p} + \nu \Delta \overline{\mathbf{u}} - \nabla \cdot \left(\overline{\mathbf{u}'\mathbf{u}'}\right) \tag{10}$$

where the unknowns are the mean velocity field $\overline{\mathbf{u}} = \overline{\mathbf{u}}(\mathbf{x},t)$ and the mean pressure field $\overline{p} = \overline{p}(\mathbf{x},t)$.

On the one hand, Eq. (9) is the differential expression of the mass balance, also known as continuity equation or incompressibility condition. On the other hand, Eq. (10) is the differential momentum balance equation referred to an Eulerian framework. The left-hand side of Eq. (10) describes the movement of the fluid: the first term is the local acceleration and the second one is the convective acceleration. The right-hand side of Eq. (10) contains the terms defining the forces acting on the fluid, where $\overline{\mathbf{u}'\mathbf{u}'}$ is the turbulent or Reynolds stress, whose analytical expression is unknown and must be determined with a statistical turbulence model.

The incompressible RANS equations are solved using an implicit, segregated, three-dimensional Finite Volume Method (FVM). Particularly, the cell-collocated implementation from the Open Source code OpenFOAM® (Weller et al. 1998) is used.

Turbulence modeling. Despite the RANS models are not the most accurate option, but the cheapest, different turbulence models from that approach are used in order to include the chaotic behavior of the flow during the simulation.

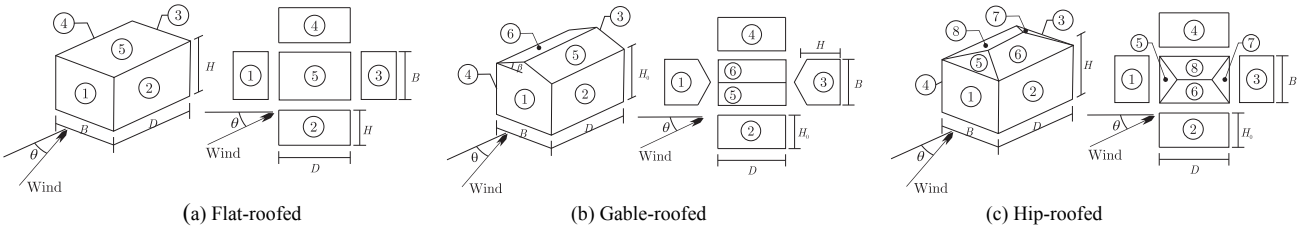

(a) Flat-roofed (b) Gable-roofed (c) Hip-roofed

Fig. 1 Building types used in the experiments of the Wind Engineering Information Center of the Tokyo Polytechnic University (TPU) (Quan et al. 2007), showing surface enumeration, the wall height H_0, the reference height H, the breadth B, the depth D, the roof angle β of the building, and the wind incidence angle θ

The fluctuating part $\mathbf{u}'$ is assumed to obey the Boussinesq hypothesis such as

$$\overline{\mathbf{u}'\mathbf{u}'} = \nu_t \nabla^S \overline{\mathbf{u}} \tag{11}$$

where ν_t is the eddy viscosity. Models based on the Boussinesq hypothesis are termed *closure models*. Most of these models estimate μ_t solving transport equation for turbulent variables like the kinetic turbulent energy, the dissipation rate, or the own eddy viscosity, among others. In this section, several popular turbulence models are compared with the aim of determining which one is the best suited for estimation of the $\overline{C_p}$ in buildings.

A family of models solving transport equations for kinetic turbulent energy k and dissipation rate ϵ are the k-ϵ models. Particularly, for comparison among the most popular turbulence models the standard k-ϵ model (Sk-ϵ) (Jones and Launder 1972), the realizable k-ϵ model (Rk-ϵ) (Shih et al. 1995), the renormalization group k-ϵ model (RNB) (Yakhot et al. 1992) and the MMK model (Tsuchiya et al. 1997) were chosen. The latter is not native of OpenFOAM®. We implemented it in OpenFOAM® taking advantage of the free access code (via the GNU-GPL license) and the modularity of its library.

Another family of closure models, having k and the specific rate of dissipation ω as unknown, are the k-ω models. Among them, the standard model (Sk-ω) and the shear stress transport formulation (SST) (Menter 1992) are selected for the current comparison analysis.

Finally, the Spalart Allmaras model (SA) was also chosen for this assessment, which is a one-equation model designed for aerospace applications involving wall-bounded flows that solves a transport equation for the kinematic eddy turbulent viscosity $\tilde{\nu}$ (Spalart and Allmaras 1992).

Geometry discretization. Computational models are made of the real scale buildings during the wind-tunnel measurements. The dimensions of the computational domain are chosen based on the best practice guidelines proposed by Cośtola and Alucci (2011), i.e., the domain height is five times the building height H, while the distance in the remaining directions is at least $10H$, see Fig. 2(a). In order to be able to correctly impose the boundary conditions, the external limit of the domain is represented by a regular polygon of eight sides, giving the possibility of selecting inflow wind directions every 45°. Figure 2(a) schematically represents the external boundaries.

To generate the computational grids, the *snappyHexMesh* (OpenCFD 2004) tool is employed. For each case, the triangulated building surface geometry is generated along with the triangulated surface geometry of the far-field polygon. Then, an iterative process generates the final mesh starting from a base mesh and morphing the resulting split-hex mesh to the surfaces. An optional phase shrinks back the resulting mesh and inserts clustered cells (layers) towards the walls. The hex-dominant volumetric meshes created in the current case have volumetric refinement near the building. Moreover, boundary layers are used on every building surface, and also over the lower boundary of the domain (ground). Figures 2(b), (c) and (d) show the generated grids for the flat-, gable- and hip-roofed cases (the same mesh is employed for any incidence angle). Resulting meshes have 500 K,

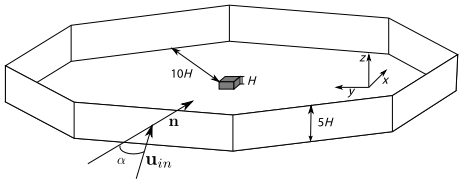

(a) External regular polygon with eight planes

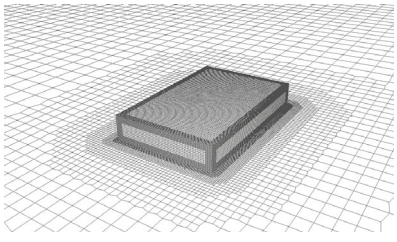

(b) Flat-roofed case with H/B = 1:4, D/B = 3:2 and β = 0°

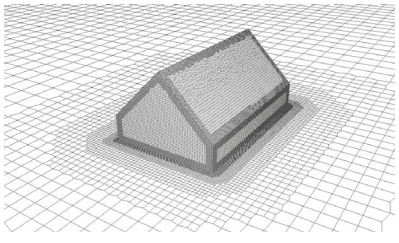

(c) Gable-roofed case with H/B = 1:4, D/B = 3:2 and β = 45°

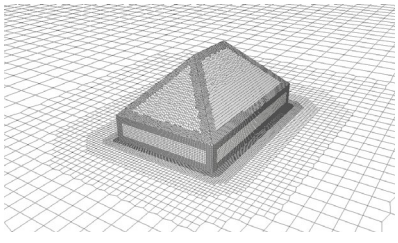

(d) Hip-roofed case with H/B = 1:4, D/B = 3:2 and β = 45°

Fig. 2 Domain boundary representation and computational grid on the building and ground surfaces

800 K, and 780 K polyhedral cells, respectively.

Before choosing these meshes, a grid sensitivity analysis was performed (not included in this work for the sake of conciseness). From it, it was concluded that the relative little change of results among solutions using the same turbulence model but different grids, indicates that further refinement would not bring significant additional accuracy but would outweigh the computational cost of further refinement.

Boundary conditions. To compare CFD results with experimental data, the results for two different angles of wind direction: $\theta = 0°$ and $\theta = 45°$ were chosen from the TPU database. The boundary conditions at the planes of the external domain are modified according to the orientation of their normal pointing to inside, say $\mathbf{n}$. Being $\mathbf{u}_{in}$ the inlet velocity, if $\mathbf{u}_{in}\cdot\mathbf{n} > 0$, an inlet boundary condition is imposed; for $\mathbf{u}_{in}\cdot\mathbf{n} < 0$, the boundary is an outflow patch (zero static pressure); and for $\mathbf{u}_{in}\cdot\mathbf{n} = 0$ (i.e., $\mathbf{u}_{in}$ normal to $\mathbf{n}$), the boundary is prescribed as a symmetry condition, i.e., zero normal velocity and zero normal gradients of all variables.

An ABL based on the logarithmic law is applied at inlet patches with the aim of matching the velocity and turbulence profiles developed in the wind tunnel experiments. Therefore, the magnitude of the inlet velocity and turbulent variables k and ϵ are

$$|\mathbf{u}_{in}| = \frac{U^*}{\kappa}\ln\left((z+z_0)/z_0\right),\quad k = \frac{U^{*2}}{\sqrt{C_\mu}},\quad \epsilon = \frac{U^{*3}}{\kappa(z+z_0)} \tag{12}$$

where U^* is the friction velocity, $\kappa = 0.41$ is the von Karman's constant, $C_\mu = 0.09$ is the turbulent viscosity coefficient, z is the vertical coordinate, being $z = 0$ the ground and $z_0 = 0.04$ m the surface roughness height. The friction velocity is estimated as

$$U^* = \kappa\frac{U_{ref}}{\ln\left((z_{ref}+z_0)/z_0\right)} \tag{13}$$

where $U_{ref} = 22.4$ m/s is the velocity at the reference height $z_{ref} = 10$ m. Note that Eq. (12) only defines the inlet values for k and ϵ. The inlet values for the remaining turbulent variables (and implement into OpenFOAM® the corresponding boundary conditions) were estimated using the relationships $\omega = \epsilon/(C_\mu k)$ and $\tilde{\nu} = 0.1235 C_\mu k^2/\epsilon$, as suggested by Blocken et al. (2007).

As explained by Hargreaves and Wright (2007), if only velocity and turbulent profiles are imposed at the inlet, and even in the absence of obstructions, the ABL profile will decay along the fetch. That work also shows that the neutral ABL can be maintained along a lengthy fetch but only employing a modified wall function on the ground and applying shear stress to the top boundary of the domain (the latter could be relaxed imposing a slip condition). Such wall function, which also accounts for the surface roughness, is provided in OpenFOAM®, being the wall shear stress τ_w at ground estimated as

$$\tau_w = \frac{\rho\kappa C_\mu^{1/4} k_c^{1/2} |\mathbf{u}_c|}{\ln\left((z_c+z_0)/z_0\right)} \tag{14}$$

where the subscript c refers to the cell adjacent to the ground and z_c is the normal distance from the ground to this cell center. Reference coordinates, heights, and velocities are shown in Fig. 3.

Over the building surfaces, also a non-slip condition for the velocity is considered. In the case of models from the k-ϵ family, hybrid wall functions are employed. These boundary conditions define a turbulent kinetic energy or dissipation wall function for low- and high-Reynolds number turbulent flow cases. They operate in two modes, i.e. laminar or turbulent, depending on the computed y^+ value.

When a k-ω model is used, the applied boundary condition provides a standard wall function constraint on the turbulence specific dissipation. Standard wall functions are also used in the case of using SA turbulence model. The success in the use of wall functions depends on the positioning of cell centers near to solid boundaries. While hybrid wall functions admit a wide range of y^+ (normally, from 1 to 300 (Hargreaves and Wright 2007)), standard wall functions fail with a small y^+ (normally, < 30 , that is below the logarithmic region). Here, the distance from the center point of the wall adjacent cell to the building surface is 0.0019 m, which corresponds to an average $y^+ = 85$, which ensures that such point is placed in the logarithmic layer.

Solvers settings. Pressure-velocity coupling is solved with the SIMPLE algorithm (Ferziger and Perić 2002). The running procedure starts a steady simulation with the computational domain initialized everywhere to the free-stream conditions at the inflow boundary. First order schemes for the convective and viscous terms of the RANS equations and relaxed variables update are employed at the beginning to guarantee stability. After 250 iterations, the settings are switched to second-order accurate discretization schemes. The steady simulation continues until residuals have decreased by five orders of magnitude or up to reach 3000 iterations. In case

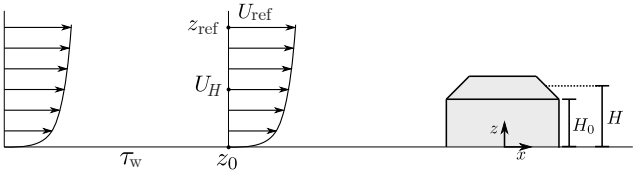

Fig. 3 ABL profile with reference heights, coordinates and velocities

of residuals convergence, the monitored data reported is taken from the last iteration.

Even using the same mesh and simulation configuration, for some wind incidence angles and/or roof types steady-state simulations do not reach the required convergence level. This cases shows that the flow cannot be treated as stationary, then a transient simulation must be carried out to obtain reliable solutions. Then, these simulations are switched to transient. Starting from the last state, ten characteristic times with variable time-step preserving a maximum Courant number $CFL_{max}<5$, are simulated. At each time-step, the residuals were required to converge three orders of magnitude. To obtain the $\overline{C_p}$ data on transient simulations, time-averaging was performed for the last period of the lowest frequency oscillation observed in the flow.

3.3 Selection of the RANS turbulence model

Regarding the CFD results analysis, the $\overline{C_p}$ for each building surface i is obtained as

$$\overline{C_p}(i) = \frac{\sum_{j=1}^{N_i} C_{p_j} A_j}{\sum_{j=1}^{N_i} A_j} \tag{15}$$

where C_{p_j} is the pressure coefficient calculated on the cell face j, A_j is the area of the cell face j, and N_i is the number of cell faces in the analyzed surface i.

In order to quantitatively measure the error of simulation results, the root mean square error (RMSE) is employed, which is defined as

$$\mathrm{RMSE} = \sqrt{\frac{1}{S}\sum_{i=1}^{S}\left(\overline{C_p}(i) - \overline{C_p}'(i)\right)^2} \tag{16}$$

where $\overline{C_p}'(i)$ is the experimental averaged pressure coefficient at surface i, and S the number of surfaces of the building case under analysis. Note that the reference height H varies depending on the roof type and the roof pitch angle β: for a building height H_0, $H = H_0$ for the flat-roofed case and $H = 0.5H_0$ for the hip- and gable-roofed cases with $\beta = 45°$. With these reference heights and considering the properties of air at 15 °C, the building Reynolds number of the computational experiments is approximately 8×10^6.

The 6 selected cases were simulated with 7 different turbulence models totalizing 42 simulations. Steady-state simulations spent approximately one hour of CPU time to reach the maximum number of iterations, while three to five hours more are needed if a transient simulation is required. The $\overline{C_p}$ for each building wall and roof was obtained and compared with experimental data.

Along years of ABL simulations, the flat-roofed was the most analyzed building shape, perhaps because of its simple geometry, which allows generating structured grids easily, and the availability of adquired data from wind tunnels and/or real scale models (Richards et al. 2007). Simulations with most of RANS turbulence models had already shown to globally agree with experiments in the prediction of flow field, but having inaccuracies in wake zones, in the pressure profiles and in the turbulence intensity. Figure 4 presents a comparison between the experimental $\overline{C_p}$ from the TPU database and the current numerically determined $\overline{C_p}$ for all the surfaces (walls and roof) of the flat-roofed case for a wind incidence angle $\theta = 0°$; the closest solution to the experimental data for each building surface is colored in green. Note that, due to the flow and geometry symmetry in this analyzed wind incidence angle, Surf-2 and Surf-4 have the same $\overline{C_p}$ values, so Surf-4 is not presented.

Tables 1 and 2 present the surface-averaged pressure coefficients for the flat-roofed cases and the two selected wind incidence angles. The $\overline{C_p}$ obtained for every surface by each turbulence model is displayed along with the experimental data and the RMSE of the simulation; for each building surface the prediction with closest value to

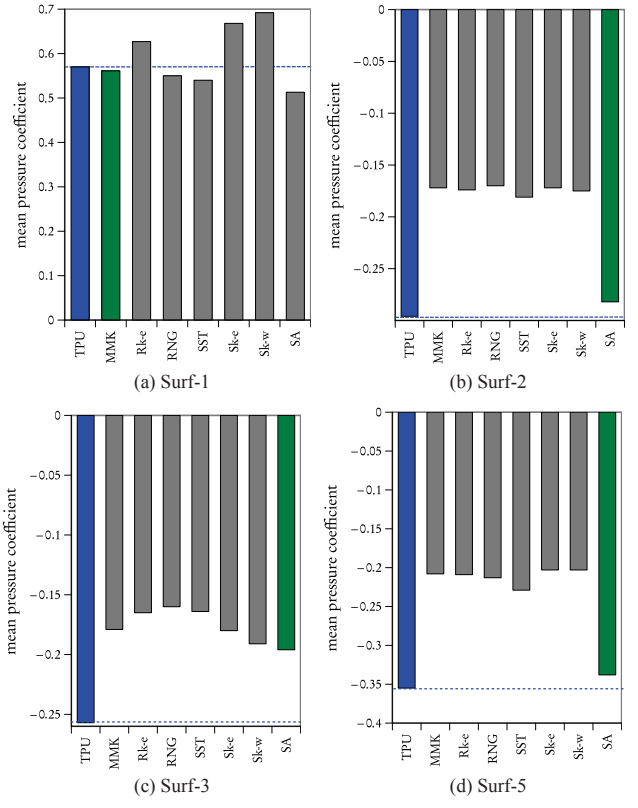

Fig. 4 $\overline{C_p}$ over the surfaces 1,2,3 and 5 for the flat-roofed case with a wind incidence angle $\theta = 0°$ using different turbulence models. The experimental data is given in blue and the most accurate simulation is in green

Table 1 $\overline{C_p}$ at every surface of the flat-roofed case with H/B = 1:4, D/B = 3:2, and an incidence wind angle θ = 0°

	Surf-1	Surf-2	Surf-3	Surf-4	Surf-5	RMSE
Experimental	0.570	-0.296	−0.257	−0.296	−0.355	—
Sk-ϵ	0.627	−0.174	−0.165	−0.174	−0.209	0.112
MMK	0.561	−0.172	−0.179	−0.172	−0.208	0.108
Rk-ϵ	0.627	−0.174	−0.165	−0.174	−0.209	0.112
RNG	0.550	−0.170	−0.160	−0.170	−0.209	0.112
Sk-ω	0.692	−0.175	−0.191	−0.175	−0.203	0.118
SST	0.540	−0.181	−0.164	−0.181	−0.229	0.102
SA	0.513	−0.282	−0.196	−0.282	−0.338	**0.039**

Table 2 $\overline{C_p}$ at every surface of the flat-roofed case with H/B = 1:4, D/B = 3:2, and an incidence wind angle θ = 45°

	Surf-1	Surf-2	Surf-3	Surf-4	Surf-5	RMSE
Experimental	0.289	0.355	−0.378	−0.448	−0.452	—
Sk-ϵ	0.335	0.379	−0.249	−0.390	−0.335	0.087
MMK	0.284	0.330	−0.243	−0.392	−0.338	0.084
Rk-ϵ	0.323	0.377	−0.228	−0.414	−0.343	0.086
RNG	0.294	0.349	−0.227	−0.399	−0.333	0.089
Sk-ω	0.374	0.420	−0.242	−0.425	−0.344	0.092
SST	0.274	0.344	−0.241	−0.449	−0.349	0.077
SA	0.231	0.314	−0.382	−0.530	−0.489	**0.051**

experimental data is underlined, while the simulation with the lowest RMSE is bold.

Regarding the k-ϵ family model predictions, conclusions from Fig. 4 and Tables 1 and 2 are similar to those found in other works (Kato and Launder 1993; Tsuchiya et al. 1997; Tominaga et al. 2015): $\overline{C_p}$ on windward sides (Surf-1 for θ = 0° and Surf-1 and Surf-3 at for θ = 45°) are overestimated by Sk-ϵ and Rk-ϵ but improved by RNG and mainly by MMK, a model conceived with this objective. On lateral and mainly leeward sides, all models largely underestimate the magnitude of the minimum $\overline{C_p}$, specially for θ = 0°. Previous conclusions can be also extended to the analyzed k-ω models, with a slight advantage to SST on leeward sides. However, the best results are those obtained by SA. Although the error using SA at the impinging side is similar to that from other models, it is noticeable how SA improves the prediction on lateral and leeward sides and roofs. For θ = 0°, SA is almost three times more accurate than any other model: it reduces the error by 62%, result pushed by the almost exact $\overline{C_p}$ prediction on the roof and Surf-2 and Surf-4 (lateral sides). This advantage is not compromised by the more complex conditions of the flow at θ = 45°, where the error using SA is approximately 33% lower than that of the best of the other models.

Regarding the other tested building cases, i.e. gable- and hip-roofed buildings with roof pitch angle β = 45° and wind incidence angles θ = 0° and θ = 45°, for the sake of conciseness, only the RMSE using each turbulence models is presented in Table 3.

In contrast to the flat-roofed case, CFD simulations with these kinds of buildings are not usually reported in the literature. With the advantage of having a lot of experimental data, an exhaustive comparison between numerical turbulence models and experiments is conducted in this work. These new cases present a more complex geometry that induces a more complex flow behavior. This affects the computational cost due to the larger number of cells in meshes and the transient behavior of the flow in most of the cases.

From these new results, it can be concluded once again that SA is the most accurate turbulence model. Neither the higher complexity of the flow nor the lower convergence ratios modify the advantage of SA against k-ϵ and k-ϵ family models. Particularly, for simulations with an oblique incidence angle, the errors with SA are reduced by around 30% to 50% comparing with those using the other tested models. The quality of the prediction of low-pressure regions on wake zones, mainly on roofs and lateral sides, is preserved even though the complex flow patterns induced by impinging angles and the unsteady nature of the solution. Although SA is still the most accurate option, its relative performance for θ = 0° is not as superior as for θ = 45°. In these cases, $\overline{C_p}$ from SA at leeward sides has the same quality than that from the others models.

Observing the RMSE values obtained for each gable- or hip-roofed simulation, it is possible to conclude that RANS models show to provide more accurate $\overline{C_p}$ predictions when perpendicular approach flow wind direction is considered, but with a little advantage to SA. However, in the case of oblique flow, larger discrepancies with the wind-tunnel measurements have been found for every model, with always less error using SA.

In the flat-roofed case, the SA gives its best performance, mainly for perpendicular flows. The one-equation SA model

Table 3 RMSE using different turbulence model on various building configurations. The lowest error option per case is framed

	Flat-roofed		Gable-roofed		Hip-roofed	
	θ=0°	θ=45°	θ=0°	θ=45°	θ=0°	θ=45°
Sk-ϵ	0.118	0.090	0.073	0.156	0.119	0.146
MMK	0.108	0.084	0.068	0.149	0.099	0.140
Rk-ϵ	0.112	0.086	0.071	0.168	0.112	0.162
RNG	0.111	0.089	0.068	0.181	0.107	0.170
Sk-ω	0.120	0.092	0.071	0.142	0.134	0.130
SST	0.102	0.077	0.060	0.151	0.105	0.147
SA	0.039	0.051	0.048	0.086	0.088	0.089

has been formulated based largely on empiricism to give the proper behavior for the mixing layers, wakes and flat-plate boundary layers typical of the flow around submerged bodies (Spalart and Allmaras 1992). Because the flow condition in flat-roof building for $\theta = 0°$ shares several features with the flow around submerged bodies at lateral and roof sides, this may be the reason to explain such prominent results. Note that on windward and leeward sides, SA results are not as good because the model was not thought for impacts or large detachments; nevertheless, accurate enough results were found along the current comparative analysis.

Therefore, being the most accurate option, SA is henceforth the chosen turbulence model for CFD prediction of $\overline{C_p}$ in buildings.

In order to validate CFD with SA turbulence model, the corresponding $\overline{C_p}$ predictions are compared to those given by the analytical S&C formula used by E+ (which is detailed in Section 4.1.1) for one of the test cases (gable-roofed with $\beta = 45°$). Figure 5 shows the comparison for the Surf-1 for wind directions θ every 15°. The CFD results present good agreement with experimental data from TPU database. Further, computing the estimation error for all these wind directions, the CFD gives RMSE=0.09 while S&C gives RMSE=0.12.

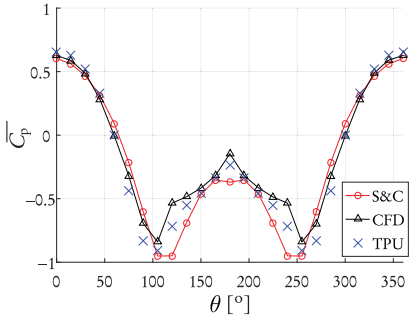

Fig. 5 $\overline{C_p}$ for Surf-1 comparing the S&C estimation and the CFD calculation with the experimental data from TPU database. Gable-roofed case with H/B = 1:4, D/B = 3:2, and $\beta = 45°$

4 Case study

Current construction practices in social housing in Argentina do not incorporate energy efficiency strategies. This seriously compromises the comfort of the occupants because these houses rarely have artificial air conditioning. The accurate modeling of the passive strategies linked with bio-climatic information would be a powerful tool in the seek of improving the thermal comfort of these kind of buildings. As mentioned before, natural ventilation is one of this strategies and has a great potential to save energy and to improve thermal comfort in Argentina, especially in the central region as it was observed by Chen et al. (2017).

The chosen case study is a detached social house of 58 m², composed of one kitchen, one living room, one bathroom, and two bedrooms, as shown in Fig. 6. The building design was though in the context of an Argentinian social housing program which is part of a governmental energy efficiency project.

4.1 Building thermal-airflow model

As mentioned before, the thermal-airflow model is implemented in E+ version 8.4.0. Each room is considered as an individual thermal zone, yielding the five zones depicted in Fig. 7. This building is located at Paraná, a city in the center of the Argentine Littoral region, with latitude 31.78° S, longitude 60.84° W and altitude 78 m. The weather data for the simulations is the typical meteorological year (TMY) recently published by Bre and Fachinotti (2016). The most occupied rooms are the bedrooms and the living room; each bedroom and the living room is assumed to be occupied by two and four people respectively, according to the schedules depicted in Fig. 8.

As internal heat sources, the occupants, the lighting and the equipment are considered. The metabolic rates for each occupant are defined as 108 W in the living room and 81 W in the bedrooms, following (ASHRAE 2009). The bedrooms and the living room have surface-mounted fluorescent luminaries. The lights in the living room and the

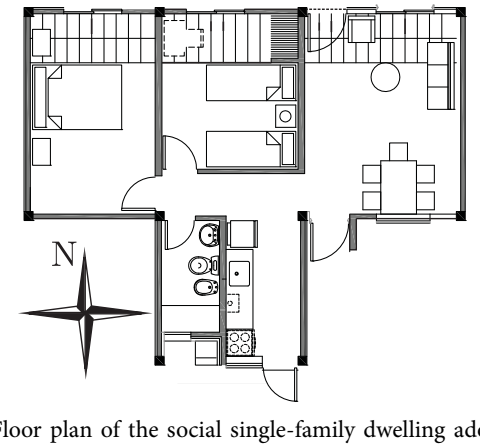

Fig. 6 Floor plan of the social single-family dwelling adopted as case study

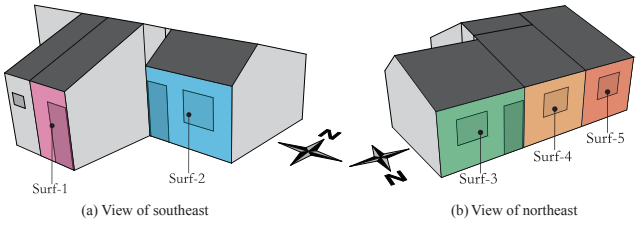

(a) View of southeast (b) View of northeast

Fig. 7 Volumetric model in 3D

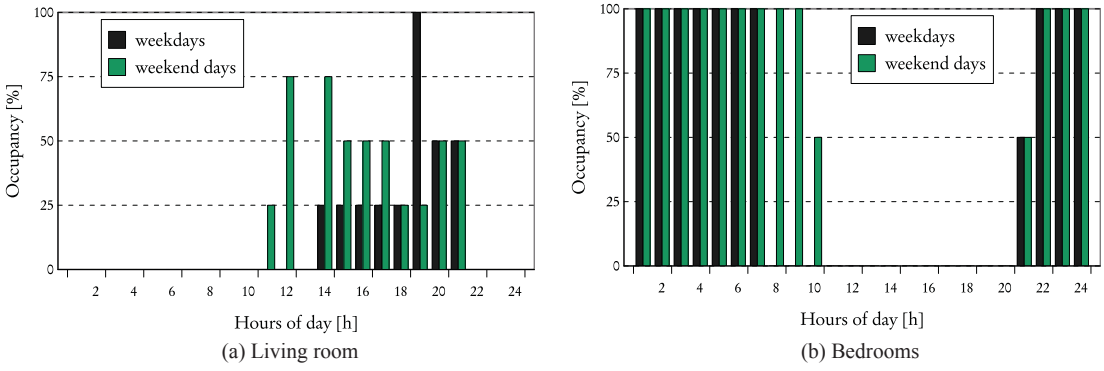

Fig. 8 Schedules of occupancy for the case study

bedrooms are turned on or off according to the corresponding schedules shown in Figs. 9(a) and (b). The lighting power density is 5 W/m^2 in the bedrooms and 6 W/m^2 in the living room. Further, the living room has electric equipment producing 1.5 W/m^2 all over the day, which has a radiant fraction of 0.72 for luminaries and 0.50 for the equipment, as suggested by ASHRAE (2009).

4.1.1 Airflow network model

The NV is modeled using the AirFlowNetwork object in E$^+$ (Gu 2007). The airflow network is composed of all the rooms except the bathroom. NV potential is evaluated during the night, when it is one of the most efficient passive cooling techniques due to the relative difference between the outdoor and indoor temperatures (Santamouris et al. 2010). Then, the windows and doors can be opened (allowing ventilation) if the outdoor temperature T_{out} is above $T_{setpoint}$ = 18 °C during the venting availability time window (08:00 p.m. –07:00 a.m.). The opening factor for the windows is 0.5 (single sliding windows) and 1 for the doors. A detailed component opening object from E$^+$ is used to specify the properties of airflow through windows and doors when they are closed or open. The discharge coefficients, which indicate the fractional effectiveness of the airflow through a window or door, are assumed to be 0.001 when the openings are closed and 0.6 when they are open. The crack flow value for closed openings is assumed to be 0.001 kg/s, and the exponent for the crack airflow equation is assumed to be 0.65.

An external node is associated to each envelope aperture with a location at the mid-wall height to define the outdoor environmental conditions. As discussed in Section 2, a key data to compute the wind-induced pressure P_W on the building surfaces (Eq. (8)) are the $\overline{C_p}$ data. Herein, because of the shape of the case study, these data are computed using the best CFD configuration (that using the *SA* turbulence model), determined in the previous section. Also, note that the wind speed used to compute P_W (Eq. (8)) is determined at the height of the centroid of each surface opening, which is specified on the Airflow Network control. The wind profile exponent to calculate the local wind speed is α = 0.22, corresponding to a suburban terrain.

$\overline{C_p}$ data by CFD. As shown in Fig. 7, the chosen case study is challenging due to its T-shape plan floor and various types of roof (a flat tilted roof and a gable roof with symmetric and asymmetric pitch angle). In order to compute $\overline{C_p}$ over each zone surface with openings (Surf-1 to Surf-5 in Fig. 7) using CFD simulations, the guidelines presented in Section 3 are followed. Regarding geometry discretization, the computational grid consists of 750 K polyhedral cells, more than 700 K of them being hexahedral. Since the building

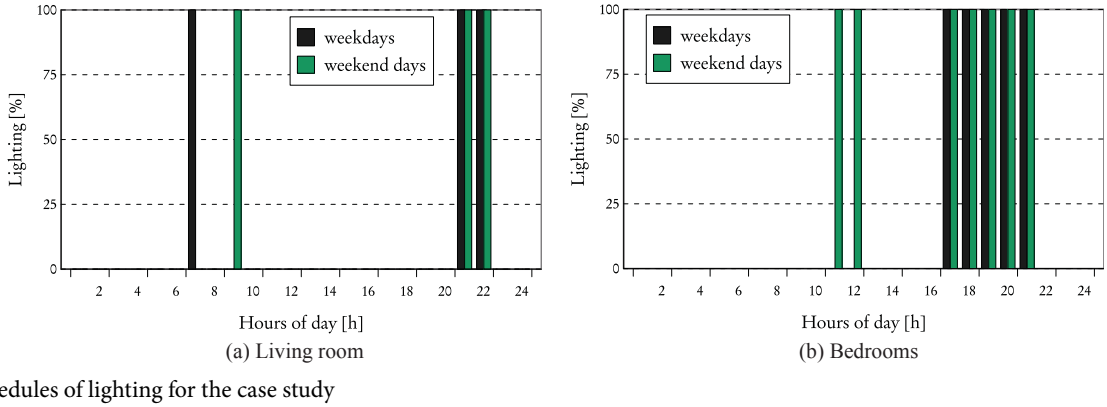

Fig. 9 Schedules of lighting for the case study

sizes are similar, the settings for the cell size of the first cell near the surface are the same as those determined in Section 3.2, and here y^+ ranges from 10 to 50. On the other hand, the external limit of the domain is now represented by a regular polygon of 24 sides, which allows to select inflow wind directions each 15°.

In order to compute $\overline{C_p}$, the mean height of the roofs is used as the reference height. The prescribed wind profile is the same as that described for the tests in Section 3.2.

For each wind incidence angle, a simulation was run following the same strategy used presented previously in tests of Section 3.3, i.e., a steady solver is started-up using relaxation and first-order schemes and, once the flow pattern has been established, it is continued with second-order schemes until convergence or switched to a transient solver. A home-made script automatically configures each simulation and distributes the execution over 12 nodes of our HPC cluster (Pirayú 2015), totalizing a computational time of only three hours. This is important to point out since it makes affordable to generate databases for different building shapes and external conditions.

$\overline{C_p}$ data by an analytical expression. To evaluate the influence of correctly calculate the $\overline{C_p}$ values, the same results are evaluated using the S&C formula for rectangular low-rise buildings, given by

$$\begin{aligned}\overline{C_p}(\theta, W_1/W_2) = \overline{C_p}(0°)\ln[1.248 - 0.703\sin(\theta/2) \\ -1.175\sin^2(\theta) + 0.131\sin^3(2G\theta) + 0.769\cos(\theta/2) \\ +0.07G^2\sin^2(\theta/2) + 0.717\cos^2(\theta/2)]\end{aligned} \quad (17)$$

where θ is the wind attack angle on the surface, and $G = \ln(W_1/W_2)$ is the natural logarithm of the ratio between the length W_1 of the side where $\overline{C_p}$ is calculated and the length W_2 of the adjacent side. Also, $\overline{C_p}$ (0°) is the $\overline{C_p}$ for $\theta = 0°$, assumed by Swami and Chandra to be equal to 0.6 independently of W_1/W_2. Therefore, the computed $\overline{C_p}(\theta, W_1/W_2)$ values for a side ratio of $W_1/W_2 = B/D = 1.205$ (see Fig. 10) and a wind angle discretization of 15° are used to feed the Airflow Network module.

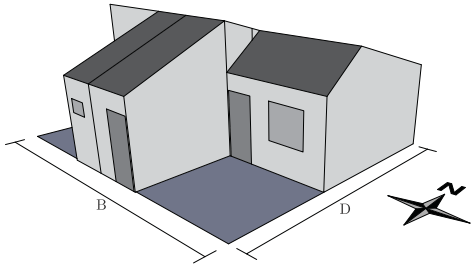

Fig. 10 Side ratio considered by S&C calculation. The same ratio of $W_1/W_2 = B/D$ is valid for both north and south sides, but the incidence angle must be shifted 180° for the south side

4.1.2 *Performance metric for natural ventilated rooms*

The impact of NV in the thermal comfort of the residents is measured using the cooling degree-hours, defined as

$$D_{cool} = \sum_h \langle T_{op}(h) - T_{upper}(h) \rangle \quad (18)$$

where $\langle x \rangle = \max(0, x)$, $T_{op}(h)$ is the operative temperature in the room at the hour h (obtained as an output of E+), and T_{upper} is the upper admissible temperature; the range of the preceding sums is a whole year, excluding the hours when the room is not occupied. The upper admissible temperature T_{upper} is defined as the upper 80%-acceptability limits (ANSI/ASHRAE 2013):

$$T_{upper} = 0.31 T_{pma(out)} + 21.3°C \quad (19)$$

where $T_{pma(out)}$ is the prevailing mean outdoor temperature, which is assumed to be the monthly mean of the local dry-bulb temperature, as shown in Fig. 11.

On the other hand, the hourly ventilation rates are measured in terms of air change per hour (ACH). This metric allows analyzing the effect of $\overline{C_p}$ on ventilation rates and, consequently, on the global thermal performance of the house.

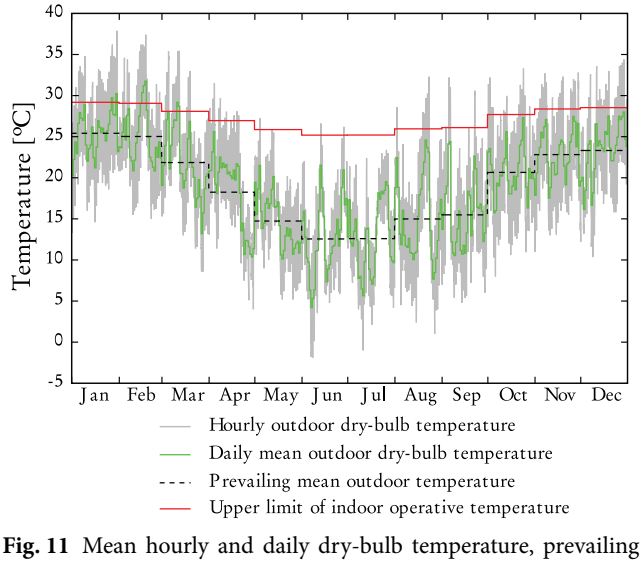

Fig. 11 Mean hourly and daily dry-bulb temperature, prevailing mean outdoor air temperature, and 80% acceptability limits for the city of Paraná

4.2 Results

4.2.1 $\overline{C_p}$ *results*

A comparison between the $\overline{C_p}$ for three building surfaces using the values predicted by the S&C formula and those obtained with CFD simulations is presented in Fig. 12. There, the differences on the estimation of the surface-averaged

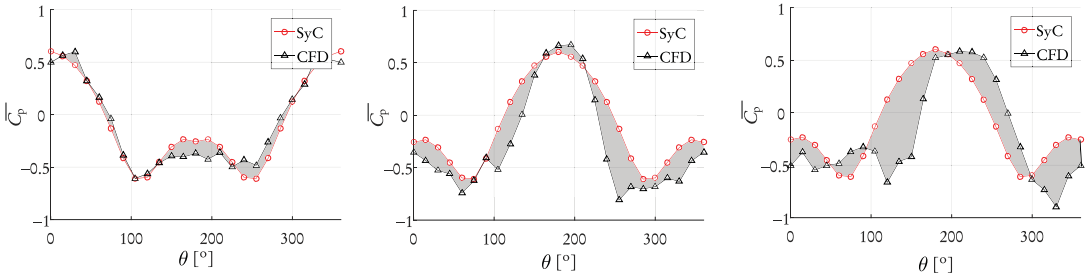

(a) Surf-1 (b) Surf-2 (c) Surf-4

Fig. 12 Surface averaged pressure coefficients for different surfaces comparing the Swamy & Chandra estimation and the CFD calculation. Differences are shadowed

pressure coefficients appear as shadowed areas, which greatly depend on the surface and the wind incidence angle.

In the case of Surf-1, which is located on the south side of the dwelling, the largest differences are found when the wind impacts directly on the surface, i.e. for θ between 90° and 270°(see Fig. 12(a)). Note that the symmetrical curve given by the S&C formula is close to the CFD prediction.

This is not the case for Surf-2 (Fig. 12(b)), where large discrepancies are found because the assumption of rectangular floor-plan adopted by the S&C formula is not applicable. For θ between 100° and 200°, Surf-2 is in the wake of the rooms attached to the main building (bathroom and kitchen), then it does not receive a direct impact of wind as it is assumed for rectangular floor-plan buildings. Actually, direct wind impact to Surf-2 occurs only for $\theta > 200°$ which leads to an asymmetric $\overline{C_p}$ curve like the one obtained with CFD.

Figure 12(c) shows the results for the central North-facing Surf-4, where the S&C estimation is in partial agreement with the CFD results. For impact wind angles (0° to 90° and 170° to 360°) both results closely agree. Some differences are found for wind angles coming from Southwest and Southeast, when the analyzed surface is in the wake of the building. Two reasons can justify this disagreement: the under-prediction of $\overline{C_p}$ by CFD on leeward sides, as discussed in Section 3, and the particular location of Surf-4, which is enclosed by Surf-3 and Surf-5, so making the flow shedding does not directly affect the pressure values over the surface.

In order to expand the discussion of the previous paragraphs, Fig. 13 presents snapshots with the CFD solution for wind directions θ = 120° and θ = 330°. In the case of southwest incidence angle (Fig. 13(a)), Surf-2 does not receive the direct impact of wind as assumed for rectangular floor-plan buildings. Instead, the surface is in the wake zone generated by the attached rooms, where low pressures are observed.

For the case of north wind incidence, at the surfaces where the wind impacts, the $\overline{C_p}$ from simulations presents a non-symmetrical curve. Particularly for the case showed in Fig. 13(b), Surf-3 has a larger $\overline{C_p}$ (0.747) because it receives direct wind impact, while Surf-4 and Surf-5 have lower $\overline{C_p}$ (0.557 and 0.326 respectively). The analytical S&C formula is not able to reproduce these different results for surfaces with the same relative wind incidence angle. Also, the complex building geometry induces a zone with very low pressure at the front of Surf-2, which is observed in Fig. 12(b) where a global minimum of $\overline{C_p}$ (−0.897) can be found. No global minimum is found at this angle if the S&C expression is used.

4.2.2 *NV results*

Three BPS simulations of the case study were carried out:

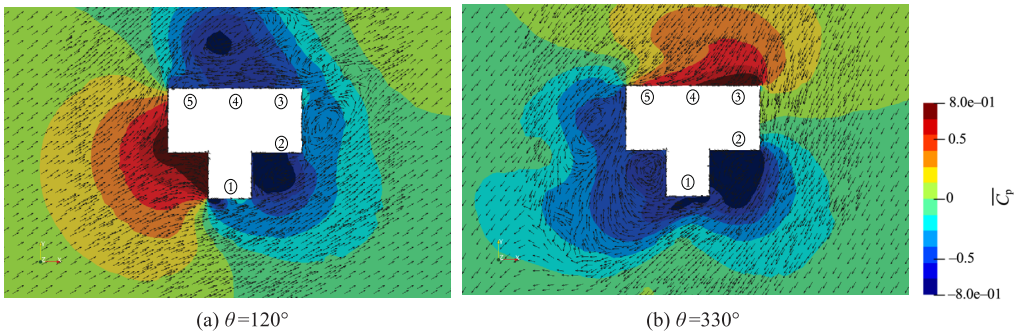

(a) θ=120° (b) θ=330°

Fig. 13 Plan slice at z = 1.5 m coloured with the pressure coefficient. Arrows indicates wind direction over the plane. Numbers indicate the Surf-i index corresponding to the specification in Fig. 7

one without including NV (NoVent), and two including NV (termed CFD and S&C according to the $\overline{C_p}$ source).

Figure 14 presents the simulations results for the air change per hour (ACH) and the operative temperature in the living room during two austral summer days (January, 27–28). Figure 14(a) shows the ACH due to natural ventilation using the different $\overline{C_p}$ source. Large dissimilarities are found when the wind direction is between west and south, i.e. $90° < \theta < 180°$. In the case of S&C, it overestimates the external airflow since it does not take into account that the openings are in the wake of the bathroom and the kitchen which act as windshields for these wind directions. In Fig. 14(b), it can be seen the effect of the dissimilar airflow estimation on the prediction of the operative temperature T_{op}. When NV is considered, a little mismatch (< 1 °C) is observed when using CFD or S&C as $\overline{C_p}$ sources, and it is even smaller during no ventilated hours. On the other hand, large differences in T_{op} are found when comparing unventilated (NoVent) and night ventilated scenarios: for NoVent, T_{op} is 3–5 °C higher for these summer days.

Moreover, without NV, T_{op} never falls below the upper admissible limit in those summer days, which is really uncomfortable for the dwelling occupants.

For better understanding, another example with a wider range of wind directions during ventilated hours is analyzed in Figs. 15 and 16 for two other austral summer days (February, 6–7). In this case, Fig. 15 presents the hourly predictions of airflow rate for the living room and one bedroom. It clearly shows that when θ is in a range of angles where larger discrepancies in $\overline{C_p}$ data were found, the differences of predicted airflow on the living room are relevant (see Fig. 15(a) for hours between 0 and 5 h). Otherwise, CFD predictions are close to S&C ones. The influence of airflow rate on $\overline{C_p}$ data is confirmed when the ACH prediction for the bedroom is observed (see Fig. 15(b)). As mentioned in the previous subsection, the analytical expression used by S&C is in relative well agreement with the CFD on north surfaces. Therefore, the fact of the bedroom has exterior openings only over these surfaces justifies that the ACH estimated by AFN model for the two ventilated scenarios is in agreement. However, a small but perceptible discrepancy is found when the wind comes from Southwest denoting that each zone cannot be individually analyzed because of the existence of internal openings connecting different zones of the multizone building model.

Figure 16 shows the operative temperature results for the living room and the bedroom for the same February days analyzed in Fig. 15. In both cases, a slight influence of

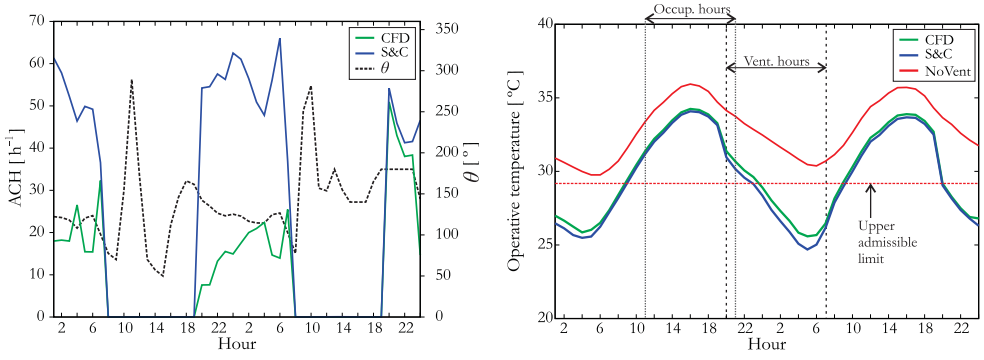

Fig. 14 BPS results in the living room during two summer days (January, 27–28). (a) ACH estimated from different $\overline{C_p}$ source; (b) Operative temperature for the different scenarios

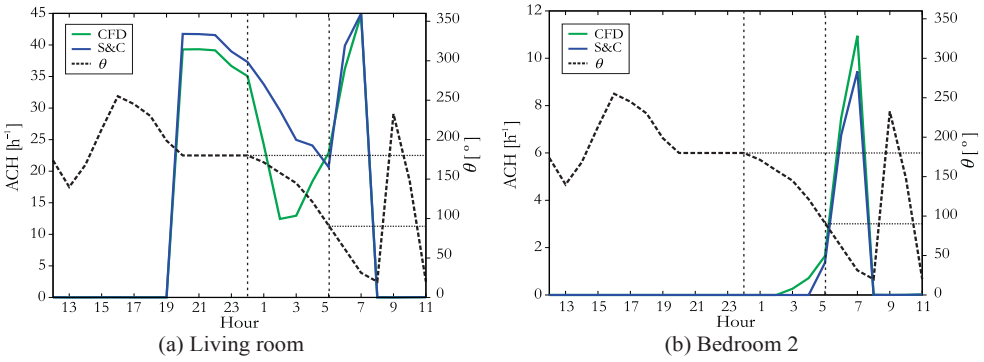

Fig. 15 ACH predictions. February, 6–7

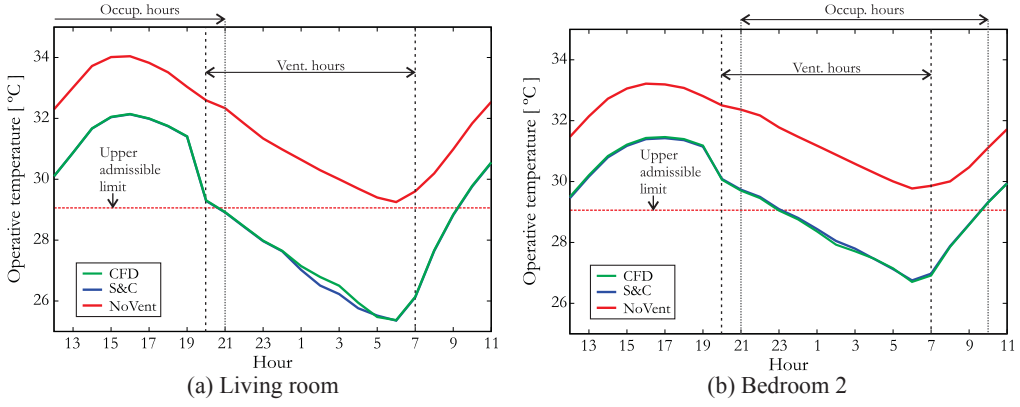

Fig. 16 Operative temperature predictions. February, 6–7

$\overline{C_p}$ data source on the thermal performance prediction of dwelling is observed. Furthermore, as was found before, great improvements in thermal performance are achieved when ventilated strategies are used in contrast with unventilated ones, even more outstood for ventilated hours.

In order to quantify the differences observed before, the cooling degrees-hours predicted using BPS without ventilation as well as with natural ventilation (and with $\overline{C_p}$ coming from either S&C or CFD) are listed in Table 4. From these results, as expected, large dissimilarities between including or not natural ventilation are noticeable. Regarding the living room, D_{cool} is reduced by 65% employing NV, while for bedrooms the difference is greater, achieving a reduction between 95% and 98%.

The larger impact on D_{cool} achievable in the bedrooms can be explained because the period of NV is during the night when the outdoor temperature is commonly lower than the indoor one, and those rooms are occupied. The current results confirm the potential of NV ventilation to improve the thermal performance of buildings and the need for including it and its modeling in the design stage. On the other hand, the prediction for ventilated scenarios using $\overline{C_p}$ data from CFD and S&C, as seen in Table 4, confirms that the thermal performance is slightly sensitive to the $\overline{C_p}$ source. This is because of the high differences found in the prediction of airflow rate for a wind angle range that do not considerably affect the annual thermal performance balance measured by degree-hours. Similar conclusions were found by Ramponi et al. (2014) for simpler geometries.

Table 4 D_{cool} in °Ch/year evaluated in three zones of the dwelling comparing three BPS: not including NV, including NV with $\overline{C_p}$ data from simulations (CFD), and including NV with $\overline{C_p}$ data from the analytical expression (S&C)

	NoVent	CFD	S&C
Living room	2344	853	835
Bedroom 1	1064	26	23
Bedroom 2	763	32	29

5 Conclusions

With the aim of presenting a comprehensive natural ventilation modeling of a non-rectangular floor-plan social dwelling located in the Argentine Littoral region, a CFD-BPS pipeline was developed. CFD simulations, which were previously calibrated, were applied to determine the surface-averaged pressure coefficients ($\overline{C_p}$) over the dwelling surfaces with openings for a set of wind incidence angles. Then, these data were used to feed a building thermal-airflow performance analysis, for a typical meteorological year, to model the effect of the natural ventilation strategy on the thermal performance. Further, the impact of $\overline{C_p}$ data sources, either CFD or Swamy & Chandra parametric equation, in terms of air change per hours and cooling degree-hours, was evaluated. an buildings A key feature of the CFD settings calibration was the selection of a proper RANS turbulence model. To this end, the $\overline{C_p}$ on building surfaces obtained from experimental data on several cases (varying wind incidence angles and roof types) and the prediction of 3D CFD simulations were comprehensively studied and compared.

The main contributions of this work are summarized below:

- It was found that the Spalart-Allmaras turbulence model is the best suited choice to compute $\overline{C_p}$ on low-rise building surfaces. The prediction using this model was found to have 15% and 60% less error, in terms of root mean square, than the second best options in the worst (hip-roofed) and in the best (flat-roofed) cases, respectively. Therefore, after the current exhaustive study, the use of CFD with the Spalart-Allmaras turbulence model is recommended to simulate the atmospheric boundary layer with the final aim of computing $\overline{C_p}$ on low-rise buildings.

- The building performance simulation results confirmed that the natural ventilation is a relevant strategy to improve the thermal comfort, reducing the cooling degree hours by 65% in the living room and at least 95% in bedrooms, compared with the unventilated case.
- Moreover, in concordance with other works where simpler geometries were studied, it was found that the sensitivity of the cooling degree-hours with respect to $\overline{C_p}$ data source is not critical.
- On the other hand, large dissimilarities were found when the hourly ventilation rates were analyzed for a particular wind angles incidence range. Although the differences in airflow rate calculations did not considerably impact on the thermal performance of the case study, this aspect could be highly influential for the evaluation of air quality indices, which we are planning to study in future works. So, the need for suitable estimations of pressure coefficients data is still a requirement for natural ventilation studies.

As future research, we aim to validate the application of the current methodology to other cases, either with different typologies (like offices and multifamily residential buildings) or different building shapes (U-shape, L-shape, high-rise, etc.) with or without surroundings conditions.

Attending to the sensitivity of the predicted ventilation rate to $\overline{C_p}$ data, it is necessary to generate $\overline{C_p}$ databases for typical but more complex building shapes like U-shape, L-shape, H-shape, etc. applying the CFD configuration selected in this work. Also, new calibrated RANS models, using experimental data, could be developed to improve the prediction of both $\overline{C_p}$ and C_p distribution on specific building applications.

Acknowledgements

For funding this work, we would like to thank Universidad Nacional del Litoral via CAI+D 2016 PJ 50020150100018LI. Also, we would like to thank the Agency for Science, Technology and Innovation (ASaCTeI) of the Province of Santa Fe (Argentina) via the Research Project 2010-022-16 "Optimization of the energy efficiency of buildings in the Province of Santa Fe". The present work uses the computational resources of the Pirayú group, acquired with funds from ASaCTeI through Project AC-00010-18, Resolution N° 117/14. This equipment is part of the National System of High Performance Computing of the Argentine Ministry of Science and Technology.

References

ANSI/ASHRAE (2013). American National Standards Institute (ANSI) and American Society of Heating, Refrigerating and Air-Conditioning Engineers (ASHRAE) Standard 55-2013. Thermal Environmental Conditions for Human Occupancy.

ASHRAE (2009). ASHRAE Handbook—Fundamentals. Atlanta, GA, USA: American Society of Heating, Refrigerating and Air-Conditioning Engineers.

Blocken B, Stathopoulos T, Carmeliet J (2007). CFD simulation of the atmospheric boundary layer: Wall function problems. *Atmospheric Environment*, 41: 238–252.

Bre F, Fachinotti VD (2016). Generation of typical meteorological years for the Argentine Littoral Region. *Energy and Buildings*, 129: 432–444.

Bre F, Fachinotti VD (2017). A computational multi-objective optimization method to improve energy efficiency and thermal comfort in dwellings. *Energy and Buildings*, 154: 283–294.

Bre F, Gimenez JM, Fachinotti VD (2018). Prediction of wind pressure coefficients on building surfaces using artificial neural networks. *Energy and Buildings*, 158: 1429–1441.

Breesch H, Janssens A (2010). Performance evaluation of passive cooling in office buildings based on uncertainty and sensitivity analysis. *Solar Energy*, 84: 1453–1467.

Chen Y, Tong Z, Malkawi A (2017). Investigating natural ventilation potentials across the globe: Regional and climatic variations. *Building and Environment*, 122: 386–396.

Cóstola D, Blocken B, Hensen JLM (2009). Overview of pressure coefficient data in building energy simulation and airflow network programs. *Building and Environment*, 44: 2027–2036.

Cóstola D, Blocken B, Ohba M, Hensen J (2010). Uncertainty in airflow rate calculations due to the use of surface-averaged pressure coefficients. *Energy and Buildings*, 42: 881–888.

Cóstola D, Alucci MP (2011). Aplicação de CFD para o cálculo de coeficientes de pressão externos nas aberturas de um edifício. *Ambiente Construído*, 11: 145–158.

Crawley DB, Lawrie LK, Winkelmann FC, Buhl WF, Huang YJ, Pedersen CO, Strand RK, Liesen RJ, Fisher DE, Witte MJ, et al. (2001). EnergyPlus: Creating a new-generation building energy simulation program. *Energy and buildings*, 33: 319–331.

de Dear RJ, Brager GS (2002). Thermal comfort in naturally ventilated buildings: Revisions to ASHRAE Standard 55. *Energy and Buildings*, 34: 549–561.

Ferziger JH, Perić M (2002). Computational Methods for Fluid Dynamics, 3rd edn. New York: Springer.

Filippín C, Ricard F, Flores Larsen S, Santamouris M (2017). Retrospective analysis of the energy consumption of single-family dwellings in central Argentina. Retrofitting and adaptation to the climate change. *Renewable Energy*, 101: 1226–1241.

Grosso M (1992). Wind pressure distribution around buildings: A parametrical model. *Energy and Buildings*, 18: 101–131.

Gu L (2007). Airflow network modeling in EnergyPlus. In: Proceedings of the 10th International IBPSA Building Simulation Conference, Beijing, China.

Hargreaves DM, Wright NG (2007). On the use of the k-ε model in commercial CFD software to model the neutral atmospheric boundary layer. *Journal of Wind Engineering and Industrial Aerodynamics*, 95: 355–369.

Hong T, Langevin J, Sun K (2018). Building simulation: Ten challenges. *Building Simulation*, https://doi.org/10.1007/s12273-018-0444-x.

Intergovernmental Panel on Climate Change (2014). Climate Change 2014: Impacts, Adaptation, and Vulnerability. Part B: Regional Aspects. Contribution of Working Group II to the Fifth Assessment Report of the Intergovernmental Panel on Climate Change. Cambridge, UK: Cambridge University Press.

Invidiata A, Ghisi E (2016). Impact of climate change on heating and cooling energy demand in houses in Brazil. *Energy and Buildings*, 130: 20–32.

Jones WP, Launder BE (1972). The prediction of laminarization with a two-equation model of turbulence. *International Journal of Heat and Mass Transfer*, 15: 301–314.

Kato M, Launder BE (1993). The modeling of turbulent flow around stationary and vibrating square cylinders. In: Proceedings of the 9th Symposium on Turbulent Shear Flows, pp. 10-4-1–10-4-6.

Menter FR (1992). Two-equation eddy-viscosity turbulence models for engineering applications. *AIAA Journal*, 32: 1598–1605.

Montazeri H, Blocken B (2013). CFD simulation of wind-induced pressure coefficients on buildings with and without balconies: Validation and sensitivity analysis. *Building and Environment*, 60: 137–149.

Muehleisen RT, Patrizi S (2013). A new parametric equation for the wind pressure coefficient for low-rise buildings. *Energy and Buildings*, 57:245–249.

Murakami S (1998). Overview of turbulence models applied in CWE-1997. *Journal of Wind Engineering and Industrial Aerodynamics*, 74: 1–24.

Murakami S, Mochida A, Hayashi Y (1990). Examining the k-ϵ model by means of a wind tunnel test and large-eddy simulation of the turbulence structure around a cube. *Journal of Wind Engineering and Industrial Aerodynamics*, 35: 87–100.

Ntinas GK, Shen X, Wang Y, Zhang G (2018). Evaluation of CFD turbulence models for simulating external airflow around varied building roof with wind tunnel experiment. *Building Simulation*, 11: 115–123.

OpenCFD (2004). OpenFOAM Programmer's Guide. Springer.

Orme M, Leksmono N (2002). AIVC Guide 5: Ventilation modelling data guide. International Energy Agency, Air Infiltration Ventilation Center. AIC-GUI, 5.

Oropeza-Perez I, Østergaard PA (2014). The influence of an estimated energy saving due to natural ventilation on the Mexican energy system. *Energy*, 64: 1080–1091.

Pirayú (2015). Pirayú cluster. Available at http://www.cimec.org.ar/c3/pirayu. Accessed 15 May2015.

Quan Y, Tamura Y, Matsui M, Cao S, Yoshida A (2007). TPU aerodynamic database for low-rise buildings. In: Proceedings of the 12th International Conference on Wind Engineering.

Rackes A, Melo AP, Lamberts R (2016). Naturally comfortable and sustainable: Informed design guidance and performance labeling for passive commercial buildings in hot climates. *Applied Energy*, 174: 256–274.

Ramponi R, Angelotti A, Blocken B (2014). Energy saving potential of night ventilation: Sensitivity to pressure coefficients for different European climates. *Applied Energy*, 123: 185–195.

Richards PJ, Hoxey RP, Connell BD, Lander DP (2007). Wind-tunnel modelling of the Silsoe Cube. *Journal of Wind Engineering and Industrial Aerodynamics*, 95: 1384–1399.

Santamouris M, Sfakianaki A, Pavlou K (2010). On the efficiency of night ventilation techniques applied to residential buildings. *Energy and Buildings*, 42: 1309–1313.

Sarinelli R, Clucellas P (2015). Boletín Official de la República Argentina [Argentine Official Gazzette] decreto 134/2015: Emergencia energética [Decrete 134/2015: Energy emergency]. (in Spanish)

Seppänen O, Fisk WJ (2002). Association of ventilation system type with SBS symptoms in office workers. *Indoor Air*, 12: 98–112.

Shih T-H, Liou WW, Shabbir A, Yang Z, Zhu J (1995). A new k-ϵ eddy viscosity model for high Reynolds number turbulent flows. *Computers Fluids*, 24: 227–238.

Sorgato MJ, Melo AP, Lamberts R (2016). The effect of window opening ventilation control on residential building energy consumption. *Energy and Buildings*, 133: 1–13.

Spalart P, Allmaras S (1992). A one-equation turbulence model for aerodynamic flows. In: Proceedings of the 30th Aerospace Sciences Meeting and Exhibit, Aerospace Sciences Meetings.

Swami MV, Chandra S (1988). Correlations for pressure distribution on buildings and calculation of natural-ventilation airflow. *ASHRAE Transactions*, 94(1): 243–266.

Tominaga Y, Akabayashi S, Kitahara T, Arinami Y (2015). Air flow around isolated gable-roof buildings with different roof pitches: Wind tunnel experiments and CFD simulations. *Building and Environment*, 84: 204–213.

Tsuchiya M, Murakami S, Mochida A, Kondo K, Ishida Y (1997). Development of a new k-ε model for flow and pressure fields around bluff body. *Journal of Wind Engineering and Industrial Aerodynamics*, 67: 169–182.

Walton GN (1989). AIRNET: A computer program for building airflow network modeling. Gaithersburg, MD, USA: National Institute of Standards and Technology.

Weller HG, Tabor G, Jasak H, Fureby C (1998). A tensorial approach to computational continuum mechanics using object-oriented techniques. *Computers in Physics*, 12: 620–631.

Wright NG, Easom GJ (2003). Non-linear k-ε turbulence model results for flow over a building at full-scale. *Applied Mathematical Modelling*, 27: 1013–1033.

Yakhot V, Orszag SA, Thangam S, Gatski TB, Speziale CG (1992). Development of turbulence models for shear flows by a double expansion technique. *Physics of Fluids A: Fluid Dynamics*, 4: 1510–1520.

Yi YK, Feng N (2013). Dynamic integration between building energy simulation (BES) and computational fluid dynamics (CFD) simulation for building exterior surface. *Building Simulation*, 6: 297–308.

Zhai Z (2014). Computational fluid dynamics applications in green building design. In: Al-Baghdadi MARA (Ed), Computational Fluid Dynamics Applications in Green Design. International Energy and Environment Foundation (IEEF), pp. 1–22.

Zhai Z, Mankibi ME, Zoubir A (2015). Review of natural ventilation models. *Energy Procedia*, 78: 2700–2705.